J Mater Sci (2013) 48:6509–6518
DOI 10.1007/s10853-013-7447-x

Preparation and characterization of nanosized magnesium ferrite powders by a starch-gel process and corresponding ceramics

Roberto Köferstein · Till Walther · Dietrich Hesse · Stefan G. Ebbinghaus

Received: 22 March 2013 / Accepted: 14 May 2013 / Published online: 30 May 2013

Abstract The synthesis and characterization of nanosized $MgFe_2O_4$ by a starch-gel method is described herein. A phase-pure nanosized $MgFe_2O_4$ powder (**1a**) was obtained after calcining a (MgFe)-starch gel at 550 °C. The powder has a specific surface area of 60.6 m^2/g and a crystallite size of 9 nm. TEM investigations reveal particles in the range of 7–15 nm. The activation energy of the crystallite growth process was calculated as 89 ± 14 kJ/mol. The shrinkage and sintering behaviour of resulting compacts were studied. UV–Vis investigations of the nanosized powder **1a** reveal an optical band gap of 2.38 eV, whereas calcination at 1100 °C (powder **1g**) leads to a crystallite size of 129 nm and a band gap of 2.16 eV. Magnetization loops at 300 K and the temperature dependence of both the field-cooled and the zero-field-cooled magnetization indicate a superparamagnetic behaviour. The blocking temperature for powder **1a** was determined as 140 K at a field of $H = 500$ Oe. We found different saturation magnetizations (M_s) depending on the calcination temperature. Calcination at 550 °C (**1a**) results in $M_s = 20.0$ emu/g which increases with calcination temperature to a maximum of 37.7 emu/g for powder **1e** calcined at 900 °C. Ceramic bodies sintered between 1450 and 1600 °C exhibit M_s values of 25–28 emu/g. Magnetic investigations at 10 K on powders **1a**–**1g** show hysteresis loops with coercivities up to 950 Oe, remanences to 10 emu/g and M_s values to 50.4 emu/g. Additionally, the nanoscaled powders show a shift of the hysteresis loops.

R. Köferstein (✉) · T. Walther · S. G. Ebbinghaus
Institute of Chemistry, Inorganic Chemistry, Martin-Luther-University Halle-Wittenberg, Kurt-Mothes-Strasse 2, 06120 Halle, Germany
e-mail: roberto.koeferstein@chemie.uni-halle.de

D. Hesse
Max Planck Institute of Microstructure Physics, Weinberg 2, 06120 Halle, Germany

Introduction

Magnesium ferrite ($MgFe_2O_4$) is an important functional magnetic material which crystallizes in the spinel structure type. $MgFe_2O_4$-based materials have found applications in microwave devices, computer memory chips and high-density recording media [1, 2]. $MgFe_2O_4$ can also be used as catalyst for the oxidation of styrene [3], the dechlorination of polychlorinated aromatic compounds [4], and the decomposition of carbon particulates [5]. Dom et al. [6] investigated the photocatalytic activity and Xiong et al. [7] showed a catalytic effect of magnesium ferrite in a heterogeneous Fenton-like reaction.

Furthermore, $MgFe_2O_4$ finds application as gas- and humidity sensor [8, 9], as semiconductor [10], and is also used as an inorganic pigment [11–13]. In addition it has been shown that $MgFe_2O_4$ is a promising candidate for local heat treatment in human cancer therapy [14, 15]. Okawa et al. [16] used $MgFe_2O_4$ as cathode material in a molten carbonate fuel cell (MCFC). Moreover, composite materials consisting of $MgFe_2O_4$ and $BaTiO_3$ show multiferroic properties [17].

$MgFe_2O_4$ is a soft-magnetic n-type semiconducting material with a *Néel* temperature of around 400 °C [18, 19]. The crystal structure lies between a normal spinel and an inverse spinel type and the fraction of tetrahedral sites occupied by Fe^{3+}-ions depends on the temperature [18–20]. For this reason the chemical formula of magnesium ferrite can be written as $^{T}(Mg_{1-x}Fe_x)^{O}(Mg_xFe_{2-x})O_4$, where T and O represent the tetrahedral and octahedral sites of the spinel-type structure, respectively. The

inversion parameter x reflects the fraction of iron cations occupying the tetrahedral site [18, 19].

To synthesise $MgFe_2O_4$ nanoparticles various chemical and physical approaches are reported such as high-energy ball milling [21], sol–gel [22], micelle [23, 24], polymerization/co-precipitate [5, 25, 26] and combustion methods [27]. An electrospinning procedure was published by Maensiri et al. [28].

The aim of this paper is to describe a versatile and cheap one-pot synthesis route to obtain nanosized $MgFe_2O_4$ by decomposition of a (MgFe)-gel using starch both as gellant and complexation agent. We have examined the decomposition process to $MgFe_2O_4$ via thermogravimetry (TG), mass spectroscopy (MS), and differential thermal analysis (DTA). Phase evolution and grain growth kinetics during the formation of $MgFe_2O_4$ have been investigated by X-ray powder diffraction (XRD). For the obtained powders of various particle sizes optical band gaps, magnetic properties and the sintering behaviour yielding dense compacts have also been studied.

Experimental

Material preparation

$Mg(NO_3)_2{\cdot}6H_2O$ (0.006 mol, Alfa Aesar, >98 %) and $Fe(NO_3)_3{\cdot}9H_2O$ (0.012 mol, *Merck*, ACS) were dissolved in 15 ml water. 2 g soluble starch (Sigma-Aldrich, p.a) were added and the mixture was stirred on a heating plate for 15 min at room temperature. Afterwards the temperature was raised to about 120–140 °C and the mixture was stirred and heated until it turned into a highly viscous red gel.

This (MgFe)-gel was calcined in static air at various temperatures for 2 h with a heating rate of 5 K/min to yield $MgFe_2O_4$ powders (**1a**–**1f**) with different particle sizes.

For comparative purposes, a coarse-grained $MgFe_2O_4$ powder (**2**) was prepared via the conventional mixed-oxide method. Stoichiometric amounts of Fe_2O_3 (Sigma-Aldrich, 99 %) and MgO (Sigma-Aldrich, 99 %) were well ground together in an agate mortar and fired at 1250 °C for 24 h in static air.

Table 1 summarizes the synthesis conditions of the $MgFe_2O_4$ powders.

For the sintering investigations, powder **1a** and **2** were mixed with 5 wt% of a saturated aqueous polyvinyl alcohol (PVA) solution as pressing aid and then the powders were pressed into pellets.

Characterization

XRD patterns with a step size of $2\theta = 0.01°$ were collected at room temperature on a *Bruker D8-Advanced* diffractometer, equipped with a one-dimensional silicon strip detector (LynxEye^{TM}) and operating with Cu-K_α radiation. Powder patterns were refined with the profile fitting software PowderCell [29]. Crystallite sizes were determined from the XRD line broadening using the Scherrer equation and the integral peak breadth (software suite WinXPOW [30]). The *Wilson*-equation was used to determine the strain parameter [30, 31]. Dilatometric (shrinkage) investigations were performed in a flowing synthetic air atmosphere (50 ml/min) in a *Setaram* TMA 92–16.18 dilatometer. Simultaneous TG, MS and DTA measurements in flowing synthetic air (30 ml/min) were performed using a *Netzsch* STA 449 system equipped with a quadrupole mass spectrometer ESD 100 (*InProcess Instruments*). The thermoanalytic measurements of the decomposition of the (MgFe)-gel were carried out on a sample preheated at 200 °C for 1 h. The specific surface area (BET) was determined using nitrogen five-point gas-physisorption (Nova 1000, Quantachrome Corporation). The equivalent BET particle diameters were calculated assuming a spherical or cubic particle shape [32]. ATR-Fourier transformed infrared (FT-IR) spectra were collected at room temperature using a *Bruker* Tensor 27 spectrometer equipped with a diamond ATR unit. Transmission electron microscopy (TEM) samples were prepared by dispersing the powder in alcohol under ultrasonic agitation, and collecting it onto a copper TEM grid covered with a carbon membrane. TEM images were recorded with a Philips CM20Twin at an electron energy of 200 keV. Scanning electron microscope images were recorded with a Philips XL30 ESEM (Environmental Scanning Electron Microscope). Diffuse reflectance spectra were obtained at room temperature in the range 380-1000 nm using a Perkin Elmer UV–Vis spectrometer Lambda 19. $BaSO_4$ was used as a white standard. Magnetic measurements were carried out using a PPMS 9 from Quantum Design. Hysteresis

Table 1 BET surface area, particle-/crystallite size and root-mean-square-strain (ε) of $MgFe_2O_4$ powders

Sample	Calcination procedure	S_{BET} (m^2/g)	d_{BET} (nm)[a]	d_{cryst} (nm)[b]	ε ($\times 10^3$)
1a	550 °C/2 h	60.6	22	9	5.5
1b	600 °C/2 h	39.6	34	11	3.9
1c	700 °C/2 h	19.1	70	13	3.4
1d	800 °C/2 h	6.0	223	32	1.3
1e	900 °C/2 h	3.2	418	57	0.8
1f	1000 °C/2 h	2.6	514	86	0.8
1g	1100 °C/2 h	2.3	573	129	0.8
2	1250 °C/24 h	1.1	1215	–	–

[a] Calculated from the specific surface area

[b] Volume-weighted average crystallite size (Scherrer equation)

loops were taken at 300 and 10 K with magnetic field cycling between −90 and +90 kOe. In addition, the temperature dependent magnetic moments were measured at $H = 500$ Oe in the temperature range of 5–300 K using field-cooled (FC) and zero-field-cooled (ZFC) conditions.

Results and discussion

Thermal analysis

Heating of the (MgFe)-gel at 200 °C for 1 h in air resulted in a black-brown powder. Simultaneous TG-MS and DTA investigations up to 700 °C in flowing air (heating rate: 5 K/min) were carried out on this powder (Fig. 1a). We detected a weight loss of 7.5 % up to 250 °C by the evaporation of water from the surface, due to the hygroscopic nature of the sample. The DTA curve shows a very weak endothermic signal and the MS curve has a weak signal for $m/z = 18$ (see inset in Fig. 1a). The strongly exothermic reaction between 285 and 319 °C is accompanied by a total weight loss of 49.2 %. This exothermic reaction is characterized by the evolution of CO_2, H_2O, NO_2, and NO and suggests a self-combustion-like process in which the nitrate ions act as an oxidizing agent and the (partly decomposed) starch molecules as fuel. A proceeding second weaker exothermic process is finished at 408 °C. Simultaneous MS indicated the evaporation of small amounts of CO_2, NO_2, and NO. A very slight last weight loss is completed at about 600 °C and the total weight loss accounts to 56.8 %. XRD investigations on the final brown product indicated phase-pure cubic $MgFe_2O_4$ [33].

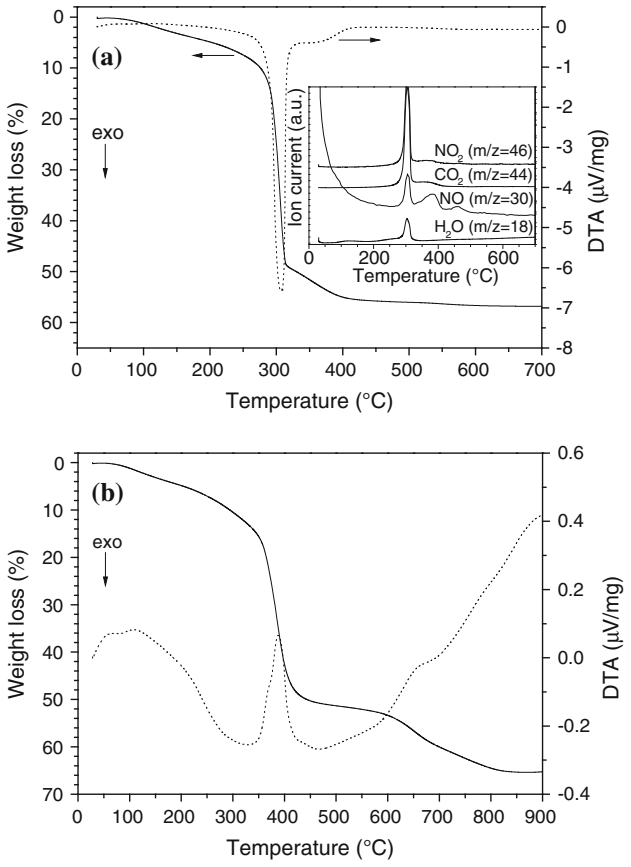

Fig. 1 Simultaneous TG-MS and DTA investigations (heating rate 5 K/min) of a preheated (MgFe)-gel in air (**a**). The *inset* in **a** shows the corresponding MS signals. TG/DTA curves in argon atmosphere (**b**)

Figure 1b shows TG/DTA measurements of the same powder as above but in argon atmosphere and up to 900 °C (heating rate: 5 K/min). Up to 500 °C, we observed a weight loss of 51.3 %. XRD investigation of the black intermediate at 500 °C revealed weak reflections of FeO and elemental iron [33]. A last decomposition process between 570 and 830 °C led to a total weight loss of 64.0 %. The decomposition processes are accompanied by two endothermic signals. In contrast to the thermoanalytic measurements in air the decomposition in argon atmosphere results in a mixture of $MgFe_2O_4$, $Mg_{1-x}Fe_xO$ [33] and elemental iron. The formation of both elemental iron and $Mg_{1-x}Fe_xO$ was also observed in the reduction of $MgFe_2O_4$ with H_2 [34]. The decomposition in argon atmosphere shows that atmospheric oxygen is essential for that combustion-like decomposition process to prepare phase-pure $MgFe_2O_4$.

XRD, TEM, IR

Figure 2 shows the phase evolution during the thermal decomposition of the red (MgFe)-gel. For these XRD investigations the samples of the (MgFe)-gel were heated

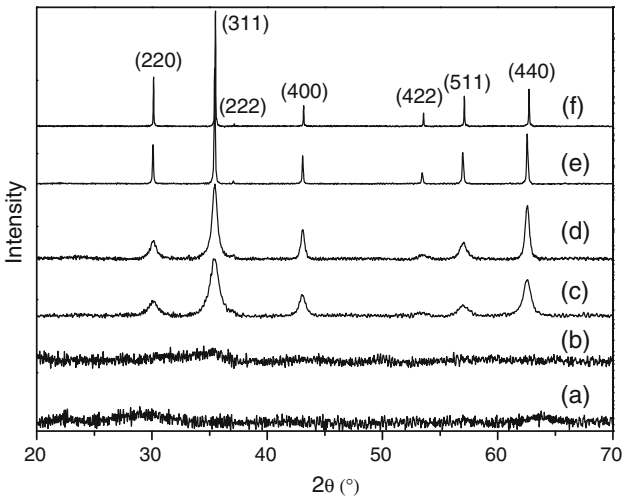

Fig. 2 Room temperature XRD patterns of the (MgFe)-gel (*a*) and resulting calcination products (*b–f*) at various temperatures (soaking time 2 h, rate 5 K/min): *b* 400 °C, *c* 550 °C (powder **1a**), *d* 700 °C (powder **1c**), *e* 1000 °C (powder **1f**). Graph *f* shows the XRD pattern of powder **2**

in a muffle furnace in static air at various temperatures for 2 h (heating rate 5 K/min) resulting in fluffy powders. The as-prepared (MgFe)-gel is X-ray amorphous (Graph 2a). Up to a calcination temperature of 400 °C we obtained only a weak and broad reflection around $2\theta \approx 35°$ possibly due to the presence of Fe_2O_3 [33]. Broad reflections of pure cubic $MgFe_2O_4$ [33] appeared after a thermal treatment at 550 °C (Graph 2c). The resulting powder (**1a**) has a BET specific surface area of 60.6 m^2/g corresponding to an equivalent particle size of 22 nm, which can be considered as the average size of the primary particles [35]. The volume-weighted average crystallite size (Scherrer equation) was calculated to be 9 nm. According to the Wilson-equation [31] the root-mean-square strain was found to be 5.5×10^3 (see also Table 1). The calculated crystallite size is roughly by the factor two smaller than the size of the primary particles obtained from the BET data because the calcination procedure of the (MgFe)-gel leads to closely joined crystallites and surface areas unavailable for nitrogen adsorption [32]. TEM investigations (Fig. 3) of powder **1a** mainly show particles in the range of 7–15 nm as well as a small fraction of larger particles up to 20 nm. Graph 2d, e exemplarily show XRD patterns of powders **1c** and **1f** calcined at 700 and 1100 °C, respectively. With higher calcination temperature the resulting powders show a decreasing specific surface area and increasingly crystallite sizes. The root-mean-square-strain is reduced with raising calcination temperature and is almost constant from 900 to 1100 °C (see Table 1).

The kinetics of crystallite growth can be expressed by the following phenomenological Eq. (1) [36]:

$$D^m - D_0^m = kt \cdot \mathrm{e}\frac{-E_\mathrm{A}}{RT} \tag{1}$$

where D_0 is the initial crystallite size, D the crystallite size after calcination for the time t and at temperature T, k is the pre-exponential constant, m the crystallite growth exponent, E_A the activation energy for the crystallite growth process and R the universal gas constant.

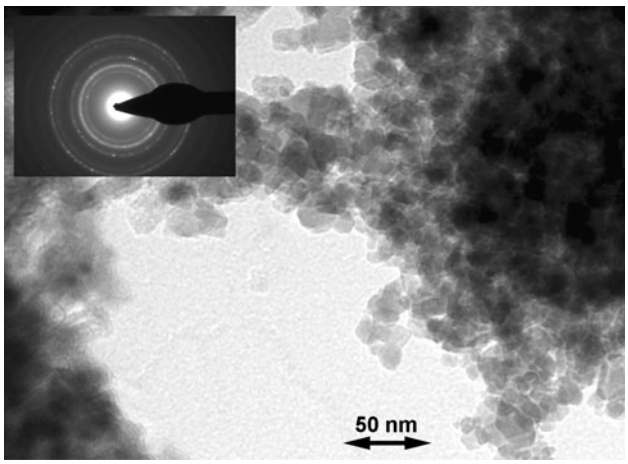

Fig. 3 TEM image of powder **1a**

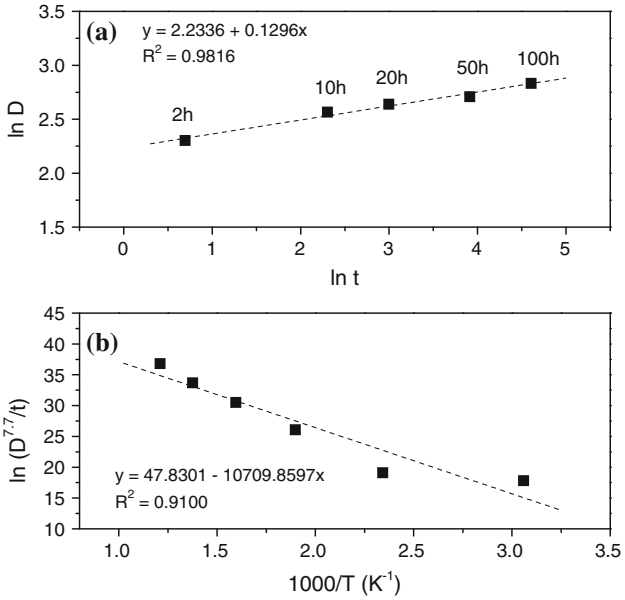

Fig. 4 **a** ln D (crystallite size) versus ln t (calcination time) for $MgFe_2O_4$ calcined at 600 °C, (**b**) plot of ln ($D^{7.7}/t$) as a function of $1/T$ for samples calcined for 2 h

The initial crystallite size D_0 is usually negligibly small, therefore Eq. 1 can be simplified to:

$$D^m = kt \cdot \mathrm{e}\frac{-E_A}{RT} \tag{2}$$

The kinetic crystallite growth exponent m can be determined from the inverse slope of ln D versus ln t. For that purpose we estimated the crystallite sizes after calcining the (MgFe)-gel at 600 °C for different times from 2 h up to 100 h. From Fig. 4a the crystallite growth exponent was found to be $m = 7.7$. The activation energy of the crystallite growth process during the calcination can be calculated from the slope of an Arrhenius plot (ln $D^{7.7}/t$ vs. $1/T$) as shown in Fig. 4b. It was calculated as $E_\mathrm{A} = 89 \pm 14$ kJ/mol.

Figure 5 represents FT-IR spectra (ATR technique) of the (MgFe)-gel, corresponding calcination products at 550 °C (powder **1a**) and 1000 °C (powder **1f**). The broad band between about 3700 and 2600 cm^{-1} in the spectrum of the (MgFe)-gel (Graph 5a) is caused by O–H stretching and C–H stretching vibrations from water and starch molecules [37]. The O–H bending mode is reflected by an absorption band at 1635 cm^{-1} [38]. Anti-symmetric and symmetric N–O vibrations from NO_3^--ions appear at 1339 cm^{-1} and as a shoulder at 1042 cm^{-1} [38]. The additional shoulder at 1406 cm^{-1} represents O–C–H, C–C–H, and C–O–H bending modes from the starch [37]. C–O–H groups cause C–O stretching vibrations at 1152 cm^{-1}, whereas C–O stretching

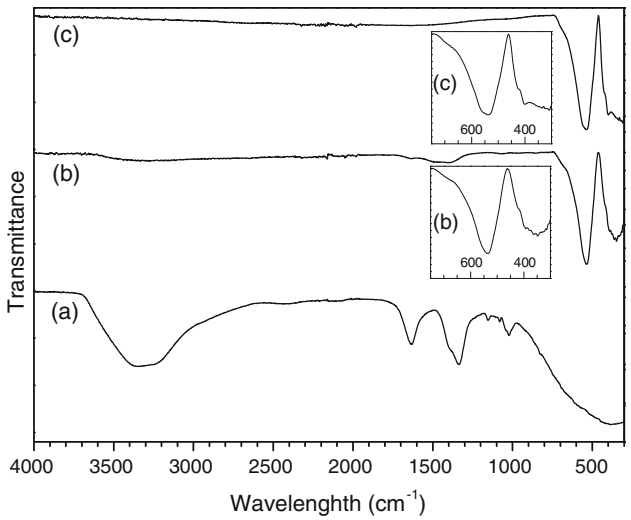

Fig. 5 FT-IR spectra (ATR technique) of (*a*) (MgFe)-gel, (*b*) powder **1a** and (*c*) powder **1f**

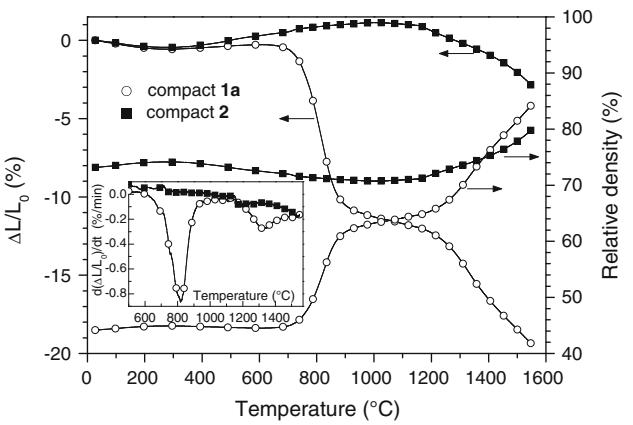

Fig. 6 Non-isothermal dilatometric measurements of green bodies of **1a** and **2** in flowing air (heating rate 10 K/min). The relative densities were calculated assuming an isotropic shrinkage behaviour. The inset shows the relative shrinkage rates (d($\Delta L/L_0$)/d*t*). The green densities are 2.0 g/cm^3 (**1a**) and 3.3 g/cm^3 (**2**), respectively

modes from C–O-C groups appear at 1080 and 1022 cm^{-1} [39].

The IR spectra of powder **1a** and **1f** show two characteristic adsorption bands v_1 and v_2 (Graph 5b, c) The higher frequency band (v_1), which appears at 539 (**1a**) and 536 cm^{-1} (**1f**) can be assigned to an iron-oxygen stretching vibration on the tetrahedral site. The lower frequency band (v_2) at 395 (**1a**) and 402 cm^{-1} (**1f**) is caused by the iron-oxygen stretching vibration on the octahedral site [40]. According to Josyulu and Sobhanadri [41], the weak absorption band at around 350 and 360 cm^{-1} (v_3) stems from a magnesium-oxygen stretching vibration on the octahedral site.

The XRD patterns of the nanopowder, **1a** was refined on the basis of a cubic unit cell (space group: Fd-3m) [42] and the cell parameter was calculated as $a = 838.40$ pm, which corresponds well to previously reported data for $MgFe_2O_4$ [18, 42].

Sintering behaviour and microstructure

Figure 6 shows the non-isothermal dilatometric investigations up to 1550 °C in flowing air (heating rate: 10 K/min). Since the green compacts **1a** (2.0 g/cm^3) and **2** (3.3 g/cm^3) strongly differ in their densities the values of the relative shrinkage are not directly comparable. Therefore, from the relative shrinkages, the evolution of the relative densities was calculated assuming an isotropic behaviour of the compacts.

The shrinkage behaviour of compact **1a** reveals a distinctive two-step characteristic. A first shrinkage process starts at about 610 °C and has a maximum of the shrinkage rate of −0.86 %/min at 820 °C. The second step begins at 1150 °C and shows a shrinkage rate maximum at 1323 (−0.28 %/min). The first step accounts to about 60 % of the total shrinkage. The rates of both shrinkage steps are more than 0.1 %/min indicating sliding processes (viscous flow) as dominant shrinkage mechanism, primarily caused by the nanoparticles [43, 44]. Between the two shrinkage steps, there is a plateau at about 950–1150 °C where the shrinkage is very small. According to investigations of Hirata et al. [45], we assume that this stage is dominated by grain growth within secondary particles (agglomerate) in such a way that almost no pores are eliminated. The final calculated relative density reaches 85 % at 1550 °C.

For comparison purposes, we also investigated a coarse-grained $MgFe_2O_4$ powder (**2**). That powder (Graph 2f) results from a conventional mixed-oxide synthesis at 1250 °C for 24 h and has a specific surface area of 1.1 m^2/g and an equivalent particle size of 1215 nm.

The shrinkage of compact **2** starts at approximately 1150 °C and a small shrinkage rate maximum of −0.09 %/min appears at 1185 °C. At about 1380 °C, the slope of the shrinkage curve changes, indicating a second shrinkage step, which is not yet finished up to 1550 °C. The sample reaches a final relative density of 80 %. Since the low shrinkage rate of compact **2** is about 0.1 %, sliding processes play no important role during the sintering. Hence diffusion processes are more relevant during the densification of the micrometre-sized compact **2** than in the nanoparticular compact **1a** [44].

The final bulk densities of ceramic bodies of **1a** after isothermal sintering at various temperatures with a soaking time of 1 and 10 h, respectively, are shown in Fig. 7. The bulk densities of the sintered bodies were calculated from their weight and geometric dimensions. The relative bulk densities (r.d.) of the ceramic bodies refer to the crystallographic density of 4.49 g/cm^3 [46]. After a soaking time

of 1 h, we obtain ceramic bodies with a relative density of 84 % at 1450 °C (grain size: 3–15 μm, Fig. 8a) and 88 % at 1500 °C (grain size: 3.5–15 μm). Dense ceramic bodies (relative density ≥90 %) form only at a sintering temperature of 1550 °C (90 %, grain size: 6–18 μm) and a relative density of 94 % is found at 1600 °C (grain size: 6–25 μm). However, a prolonged soaking time of 10 h leads to dense ceramic bodies even at 1450 °C (91 %, grain size: 4–28 μm, Fig. 8b). At 1500 and 1550 °C, the relative densities are raised to 93 and 96 % and the grain sizes are in the range of 5–42 and 16–50 μm, respectively. EDX analysis on the surface of a compact sintered for 10 h at 1550 °C reveal some grains consisting of MgO. The XRD pattern (not shown) of that ceramic shows reflections of cubic $MgFe_2O_4$ and traces of MgO. These results are consistent with investigations reported by Phillips et al. [47]. They found in samples after equilibration at ≥1500 °C besides the main phase $MgFe_2O_4$ the secondary MgO phase. Ahmed et al. [48] sintered a conventional mixed-oxide $MgFe_2O_4$ powder at 1550 °C for 2 h and obtained a ceramic body with a density of 3.71 g/cm^3 (83 %).

From these experiments it is evident that the nanocrystalline $MgFe_2O_4$ prepared from the decomposition of the starch precursor shows improved sintering properties, which is advantageous for all applications that require dense ceramics, such as in microwave devices [1, 49].

Magnetic measurements

Table 2 summarizes the magnetic data of the $MgFe_2O_4$ powders **1a**–**1g**. The evolution of magnetization (M) depending on the applied field (H) at 300 K is demonstrated in Fig. 9 for powders **1a**, **1c**, **1e** and **1g**. The saturation magnetization (M_s) was evaluated by extrapolation of the magnetization versus $1/H$ to $1/H \rightarrow 0$, according to the Law of Approach to Saturation [50]. Magnetic measurements at 300 K reveal a saturation magnetization for sample **1a** of $M_s = 20.0$ emu/g, which increases with increasing crystallite size and/or calcination

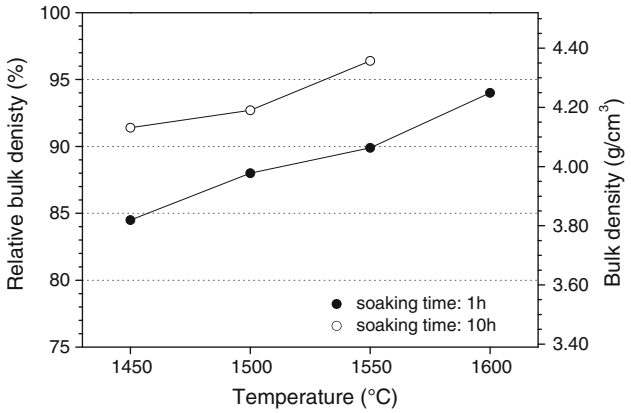

Fig. 7 Final bulk densities versus sintering temperature of ceramic bodies of **1a** (soaking time: 1 and 10 h, heating-/cooling rate: 10 K/min)

Table 2 Saturation magnetization (M_s), coercivity (H_c) and remanence (M_r) of synthesized $MgFe_2O_4$ powders at 300 and 10 K

Sample	M_s (emu/g)		H_c (Oe)		ΔH_c (Oe)[a]	M_r (emu/g)	
	300 K	10 K	300 K	10 K[b]	10 K	300 K	10 K[b]
1a	20.0	28.3	~0	950	81	~0	6.6
1b	23.0	31.8	~0	671	67	~0	7.5
1c	28.3	38.4	15.2	390	33	0.4	9.7
1d	35.5	47.4	67.2	220	11	3.0	9.5
1e	37.7	50.4	56.6	146	3.5	2.8	7.9
1f	36.9	49.5	63.4	143	3	2.9	7.5
1g	33.9	48.6	10.5	62	1	0.6	5.2

[a] Calculated from $\Delta H_c = |0.5(H_{c(df)} + H_{c(if)})|$

[b] H_c and M_r (absolute values) were determined from the decreasing field

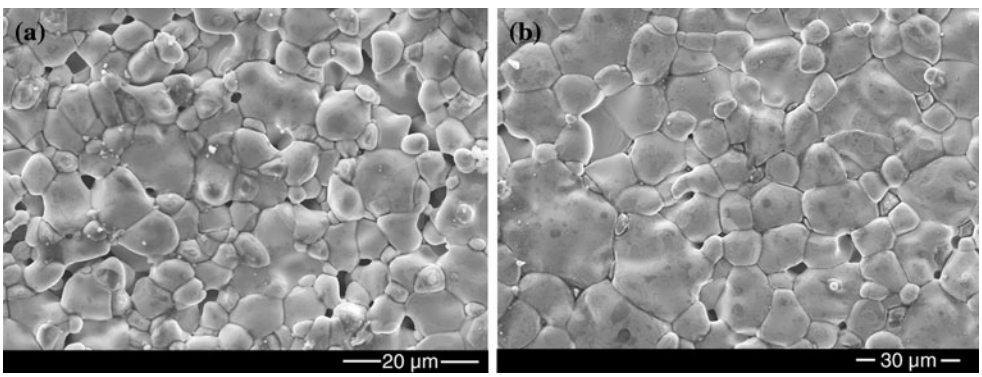

Fig. 8 SEM surface images of ceramic bodies of **1a** after isothermal sintering at 1450 °C (heating-/cooling rate: 10 K/min): **a** soaking time 1 h and **b** soaking time 10 h

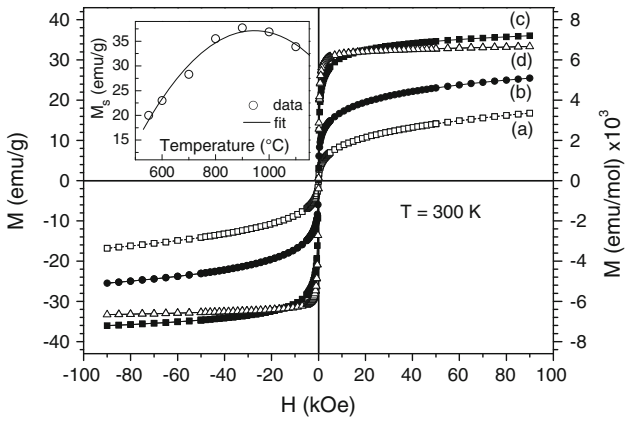

Fig. 9 Magnetization (M) versus applied magnetic field (H) of various $MgFe_2O_4$ powders at 300 K. *a* Powder **1a**, *b* powder **1c**, *c* powder **1e** and *d* powder **1g**. The *inset* shows the saturation magnetization (M_s) depending on calcination temperature

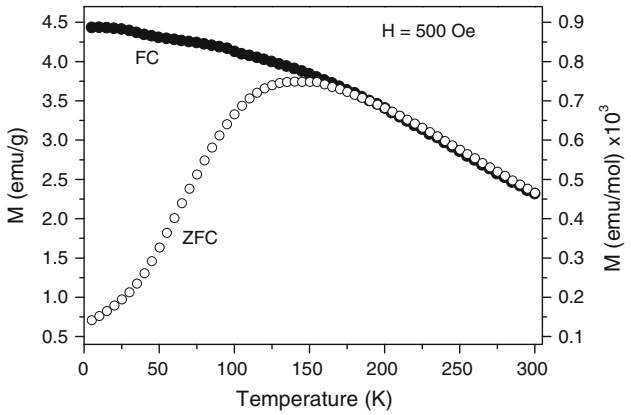

Fig. 10 Temperature dependence of the magnetization for zero-field-cooled (ZFC) and field-cooled (FC) powder **1a** in the range 5–300 K

temperature and reaches a maximum of $M_s = 37.7$ emu/g at 900 °C. Further calcinations at 1000 and 1100 °C and thus increasing crystallite sizes cause a gradual reduction of M_s (inset in Fig. 9). It is well known that among other things M_s is influenced by the crystallite size, the inversion parameter (x), and surface effects (i.e. spin-glass like behaviour of the surface spins) [23, 51]. With increasing particle size, surface effects are gradually reduced. Therefore, the reduction of M_s from crystallite sizes above 60 nm (powder **1f**, **1g**) is possibly dominated by an increase of x [51, 52].

The coercivity (H_c) and remanence (M_r) values for sample **1a** and **1b** are very small indicating a superparamagnetic behaviour [23] in accordance with the observed small crystallite sizes. The calculated M_r/M_s ratios for all samples are lower than 0.1 indicating an appreciable fraction of superparamagnetic particles at 300 K [53]. Figure 10 exemplarily shows the temperature dependence of the magnetization under ZFC and FC conditions with an

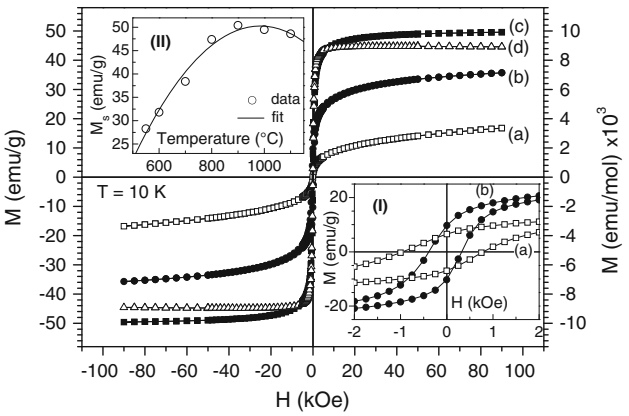

Fig. 11 Magnetization (M) versus applied magnetic field (H) of various $MgFe_2O_4$ powders at 10 K. *a* Powder **1a**, *b* powder **1c**, *c* powder **1e** and *d* powder **1g**. *Inset* (*I*) shows the saturation magnetization (M_s) depending on calcination temperature and *inset* (*II*) shows M versus H in a small field range of powders **1a** *a* and **1c** *b*

external field of 500 Oe for powder **1a**. The magnetization of the FC curve decreases with increasing temperature, while the ZFC curve increases as temperature is increased up to a maximum corresponding to the blocking temperature (T_B). Above the blocking temperature the ZFC curve starts to decrease. The formation of a maximum in the ZFC curve is a result of the superparamagnetic behaviour of the sample [54]. T_B increases with the crystallite size from 140 K for powder **1a** ($d_{cryst} = 9$ nm) to 210 K for powder **1c** ($d_{cryst.} = 13$ nm). Chen and Zhan [55] determined a blocking temperature for $MgFe_2O_4$ nanoparticles (11 nm) of about 170 K, in good accordance with values found in this work.

Below the blocking temperature, the field dependent magnetization of the $MgFe_2O_4$ powders show the formation of pronounced hysteresis loops. Figure 11 shows M-H loops at 10 K for powders **1a**, **1c**, **1e** and **1g**, exemplarily. Values of the coercivity between 950 and 60 Oe and remanences between 10.3 and 5.0 emu/g were found, indicating a ferromagnetic behaviour (inset I in Fig. 11). M_s values at 10 K are in the range from 28.3 to 50.4 emu/g, whereas the dependence of M_s on the crystallite size is analogous to the measurements at 300 K (inset II in Fig. 11). Closer inspection shows a small shift (ΔH_c) of the hysteresis loops (exchange bias-like) at 10 K of the nano-scaled $MgFe_2O_4$ powders (Table 2) in the negative direction, therefore, we found different coercivity values for decreasing and increasing field as demonstrated for powder **1a** in Fig. 12. Based on Nogues and Schuller [56] the coercivity shift is defined as $\Delta H_c = |0.5(H_{c(df)} + H_{c(if)})|$, where $H_{c(df)}$ is the coercivity at decreasing field and $H_{c(if)}$ is the coercivity at increasing field. ΔH_c describes the shift of the centre (half width) of the hysteresis loop with respect to the origin ($H = 0$). Powder **1a** with $d_{cryst} = 8$ nm has a loop shift of $\Delta H_c = 81$ Oe, which decreases with

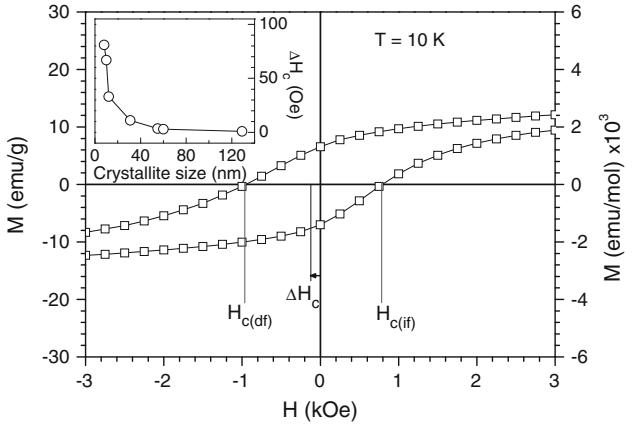

Fig. 12 Magnetization (M) versus applied magnetic field (H) of powder **1a** at 10 K in the range of small magnetic fields. The coercivity shift (ΔH_c), the coercivity at decreasing field ($H_{c(df)}$) and the coercivity at increasing field ($H_{c(if)}$) are indicated in the figure. The *inset* shows the coercivity shift (ΔH_c) depending on the crystallite size

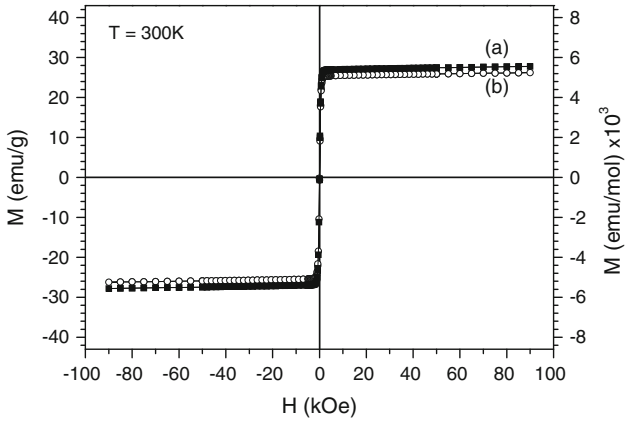

Fig. 13 Magnetization (M) versus applied magnetic field (H) of ceramic bodies from powder **1a** at 300 K. *a* Sintering at 1450 °C for 1 h and *b* sintering at 1600 °C for 1 h

increasing crystallite size (inset in Fig. 12). Loop shifts between 60 and 200 Oe were also found in high-energy milled nanocrystalline $MgFe_2O_4$ [52, 57, 58]. Loop shifts occur in materials with ferromagnetic/anti-ferromagnetic interfaces (exchange bias) [56]. Calculations on spherical NiO nanoparticles by Kodama et al. [59] showed that the loop shift originates from the interaction between the reduced coordinated surface spins and the core. According to the core–shell model by Sepelak et al. [57] we can assume that the nanocrystalline $MgFe_2O_4$ consist of a ferrimagnetic core and a surface (grain boundary) with uncompensated spins. The exchange coupling between the core and the shell leads to the observed loop shift.

M-H loops at 300 K of ceramic bodies sintered at 1450 °C for 1 h (grain size: 3–15 μm) reveal a M_s value of 28.2 emu/g, which only slightly decreases to about

Table 3 Saturation magnetization (M_s) of ceramic bodies from powder **1a** at 300 and 10 K

Sintering condition	Grain size range (μm)	M_s (emu/g)	
		300 K	10 K
1450 °C/1 h	3–15	28.2	35.9
1500 °C/1 h	3.5–15	26.5	33.5
1550 °C/1 h	6–18	25.9	32.7
1600 °C/1 h	6–25	26.6	33.4
1450 °C/10 h	4–28	27.3	34.5
1500 °C/10 h	5–42	25.3	31.8
1550 °C/10 h	16–50	26.0	32.7

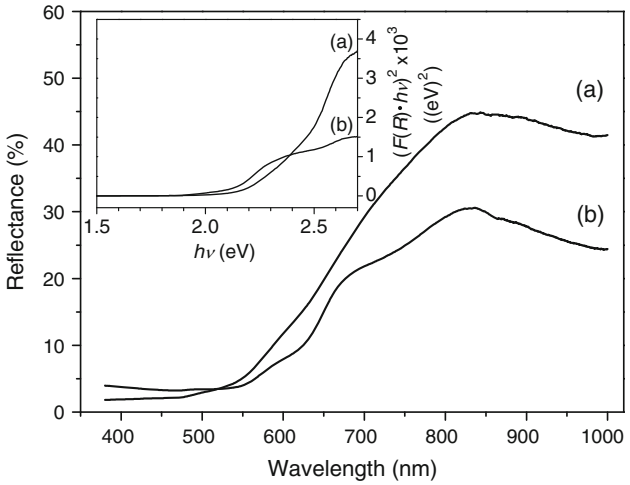

Fig. 14 Diffuse reflectance versus wavelength for powder **1a** (*a*) and a corresponding ceramic body sintered at 1450 °C for 1 h (*b*). The *inset* shows the graphical representation of $(F(R)\cdot h\nu)^2$ versus $h\nu$

26 emu/g after sintering at ≥1500 °C (Fig. 13; Table 3). Sintering for 10 h leads to the same tendency. Measurements at 10 K reveal saturation magnetizations between 32.7 and 35.9 emu/g. Coercivity and remanence of the ceramic bodies do not differ significantly from zero and indicated a blocking temperature above 300 K.

The coarse-grained powder **2** has a saturation magnetization of 28.2 emu/g at 300 K and 32.6 emu/g at 10 K and its magnetic behaviour is similar to the ceramic bodies described above. The saturation magnetizations both for the ceramic bodies and powder **2** are in good agreement with the reported M_s value of 33 emu/g at 3 K for bulk $MgFe_2O_4$ [57].

Diffuse reflectance measurements

Reported band gaps for $MgFe_2O_4$ samples are in the range of 2.0–2.2 eV [10, 60, 61]. To determine the optical band gap of $MgFe_2O_4$ diffuse reflectance spectra were recorded

in the range of 380–1000 nm, as demonstrated in Fig. 14. The samples show a high reflectance in the visible range. The Kubelka–Munk [62, 63] theory was used for the analysis of diffuse reflectance spectra as expressed by the following equation:

$$F(R) = \frac{(1-R)^2}{2R} \quad (4)$$

where $F(R)$ is the Kubelka–Munk function and R the reflectance.

The optical band gap can be determined according to Eq. 5 [64]:

$$\alpha h\nu = k(h\nu - E_g)^{1/n} \quad (5)$$

where $\propto$ is the absorption coefficient, which is proportional to $F(R)$, k is an energy-independent constant, E_g the optical band gap. The exponent n is determined by the type of transition: $n = 2$ for direct allowed transitions, $n = 2/3$ for direct forbidden transitions, $n = 1/2$ for indirect allowed transitions and $n = 1/3$ for indirect forbidden transitions.

The McLean [64, 65] analysis of the absorptions edge was applied to determine the exponent n and thus the type of transition. In the range of the absorption edge $(F(R)\cdot h\nu)^n$ versus $h\nu$ should give a straight line. We found the best choice was $n = 2$ for all samples indicating that the direct allowed transition is dominant in the samples. Hence Eq. 5 can be written as:

$$F(R) \cdot h\nu = k(h\nu - E_g)^{1/2} \quad (6)$$

The optical band gap (E_g) can be determined by plotting $(F(R)\cdot h\nu)^2$ versus $h\nu$ and extrapolating the slope to $F(R) \rightarrow 0$ as exemplarily shown in the inset in Fig. 14.

For powder **1a** (calcination at 550 °C), an optical band gap of 2.38 ± 0.05 eV was found, whereas calcination at 1100 °C (powder **1g**) lead to a reduction of the band gap to 2.16 ± 0.02 eV. The reduction is probably a result of the crystallite-/particle growth [66] (see also Table 1). The band gap energies of ceramic bodies sintered at 1450 and 1550 °C (soaking time 1 h) do not significantly differ from each other and reveal slightly lower values of 2.11 ± 0.02 eV and 2.10 ± 0.02 eV, respectively. On the other hand, the coarse-grained mixed-oxide powder **2** has a band gap of 1.91 ± 0.01 eV. The variation of the band gap with increasing particle size is an important aspect for photocatalytic applications of $MgFe_2O_4$ [6].

Conclusion

We prepared nanosized $MgFe_2O_4$ powders by decomposition of a (MgFe)-gel obtained using starch as a gellant and complexation agent. Calcining in air of the (MgFe)-gel at 550 °C leads to a nanocrystalline powder (**1a**) with crystallite sizes of 9 nm. TEM images show particles in the range of 7–15 nm. The crystallite size increases to 116 nm by calcining at 1100 °C. The activation energy for crystallite growth was found to be 89 ± 14 kJ/mol. Dilatometric measurements of compacts of **1a** show a distinctive two-step behaviour of the densification. The shrinkage starts at about 610 °C. Dense ceramic bodies with relative densities ≥90 % can be obtained after isothermal sintering at 1550 °C for 1 h and 1450 °C for 10 h, respectively. On the basis of diffuse reflectance spectra, the optical band gap of $MgFe_2O_4$ calcined at 550 °C (**1a**) was determined as 2.38 eV and was found to decrease with raising calcination temperature and in turn increasing particle size to 2.16 eV (calcination at 1100 °C, **1d**). Ceramic bodies reveal optical band gaps at 2.1 eV.

Powder **1a** shows a saturation magnetization of 20 emu/g at 300 K. Increasing calcination temperatures to 900 °C cause a raising saturation magnetization up to 37.7 emu/g, whereas *M-H* loops at 10 K reveal saturation magnetization up to 50 emu/g. We found a small shift (exchange bias) of the hysteresis loops depending on the crystallite size at 10 K. The $MgFe_2O_4$ nanosized samples show a typical superparamagnetic behaviour. They show the formation of hysteresis loops below the blocking temperature, whereas above the blocking temperature the hysteresis behaviour disappeared.

The saturation magnetization at 300 K of the obtained ceramic bodies varies only slightly with temperature and soaking time and lies between 25 and 28 emu/g.

The $MgFe_2O_4$ powders show different magnetic properties depending on their particle sizes. This offers the possibility to modify the magnetoelectric coupling phenomena in multiferroic composites. In addition, the superparamagnetic samples are potential candidates for applications as ferrofluid or contrast medium in the magnetic resonance tomography.

Acknowledgements The authors thank Dr. Th. Müller for TG/MS-DTA and Dr. L. Jäger for UV–Vis measurements. Financial support by the German Science Foundation within the Collaborative Research Centre (SFB 762) "Functionality of Oxide Interfaces" is gratefully acknowledged.

References

1. Rane KS, Verenkar VMS, Sawant PY (2008) Bull Mater Sci 24:323
2. Goldman A (2006) Modern ferrite technology. Springer Science + Business Media Inc., New York
3. Ma N, Yue Y, Hua W, Gao Z (2003) Appl Catal A 251:39
4. Ma X, Sun H, Liu W, Zheng M (2007) Fresen Environ Bull 16:745
5. Lee YH, Lee GD, Park SS, Hong SS (2005) React Kinet Catal Lett 84:311
6. Dom R, Subasri R, Radha K, Borse PH (2011) Solid State Commun 151:470

7. Xiong C, Chen Q, Lu W, Gao H, Lu W, Gao Z (2000) Catal Lett 69:231
8. Gusmano G, Montesperelli G, Nunziante P, Traversa E (1993) J Mater Sci 28:6195
9. Liu YL, Liu ZM, Yang Y, Yang HF, Shen GL, Yu RQ (2005) Sens Actuators B 107:600
10. Benko FA, Koffyberg EP (1986) Mater Res Bull 21:1183
11. Candeia RA, Souza MAF, Bernardi MIB, Maestrelli SC, Santos IMG, Souza AG, Longo E (2006) Mater Res Bull 41:183
12. Kalendová A (2000) Prog Org Coat 38:199
13. Mizoe K, Takiguchi T, Arahira F, Ito M (2005) Toner Image Form Method. US-Pat. 6897001 B2
14. Watanabe Y, Sato K, Yukumi S, Yoshida M, Yamamoto Y, Doi T, Sugishita H, Naohara T, Maehara T, Aono H, Kawachi K (2009) Bio-Med Mater Eng 19:101
15. Yukumi S, Watanabe Y, Horiuchi A, Doi T, Sato K, Yoshida M, Maehara T, Aono H, Naohara T, Kawachi K (2008) Anticancer Res 28:69
16. Okawa H, Lee JH, Hotta T, Ohara S, Takahashi S, Shibahashi T, Yamamasu Y (2004) J Power Sour 131:251
17. Tadi R, Kim YI, Sarkar D, Kim C, Ryu KS (2011) J Magn Magn Mater 323:564
18. O'Neill HStC, Annersten H, Virgo D (1992) Am Miner 77:725
19. Gateshki M, Petkov V, Pradhan SK, Vogt T (2005) J Appl Cryst 38:772
20. Harrison RJ, Putnis A (1999) Phys Chem Miner 26:322
21. Sepelák V, Bergmann I, Feldhoff A, Litterst FJ, Becker KD, Cadogan JM, Hofmann M, Hoelzel M, Wang JL, Avdeev M, Campbell SJ (2010) Hyperfine Interact 198:67
22. Berchmans LJ, Selvan RK, Kumar PNS, Augustin CO (2004) J Magn Magn Mater 279:103
23. Chandradass J, Jadhav AH, Kim H (2012) Appl Surf Sci 258:3315
24. Iqbal MJ, Ahmad Z, Melikhov Y, Nlebedim IC (2012) J Magn Magn Mater 324:1088
25. Hoque SM, Hakim MA, Mamun A, Akhter S, Hasan MT, Paul DP, Chattopadhayay K (2011) Mater Sci Appl 2:1564
26. Akhtar MJ, Younas M (2012) Solid State Sci 14:1536
27. Khot VM, Salunkhe AB, Phadatare MR, Pawar SH (2012) Mater Chem Phys 132:782
28. Maensiri S, Sangmanee M, Wiengmoon A (2009) Nanoscale Res Lett 4:221
29. Kraus W, Nolze G (1998) Powder Diffr 13:256
30. Program WinXPOW v1.06 (1999). Stoe & Cie GmbH, Darmstadt
31. Stokes AR, Wilson AJC (1994) Proc Phys Soc 56:174
32. Allred VD, Buxton SR, McBride JP (1957) J Phys Chem 61:117
33. PDF 2 (International Centre for Diffraction Data, Pennsylvania) (2001). $MgFe_2O_4$ [71–1232], Fe_2O_3 [72–469], Fe [6–696], FeO [6–615], $Mg_{1-x}Fe_xO$ [35–1393]
34. Qian YT, Kershaw R, Dwight K, Wold A (1983) Mater Res Bull 18:543
35. Buscaglia MT, Bassoli M, Buscaglia V, Alessio R (2005) J Am Ceram Soc 88:2374
36. Cun W, Xinming W, Jincai Z, Bixian M, Guoying S, Ping′an P, Jiamo F (2002) J Mater Sci 37:2989
37. Changa PR, Zheng P, Liu B, Anderson DP, Yu J, Ma X (2011) J Hazard Mater 186:2144
38. Nakamoto K (1986) Infrared and Raman spectra of inorganic and coordination compounds. Wiley, USA
39. Fang JM, Fowler PA, Tomkinson J, Hill CAS (2002) Carbohydr Polym 47:245
40. Gadkari AB, Shinde TJ, Vasambekar PN (2010) J Mater Sci Mater Electron 21:96
41. Josyulu OS, Sobhanadri J (1981) Phys Status Solid A 65:479
42. Gaudon M, Pailhe N, Wattiaux A, Demourgues A (2009) Mater Res Bull 44:479
43. Köferstein R, Jäger L, Zenkner M, Ebbinghaus SG (2009) J Eur Ceram Soc 29:2317
44. Schatt W (1992) Sintervorgänge. VDI, Düsseldorf
45. Hirata Y, Hara A, Aksay IA (2009) Ceram Int 35:2667
46. Kirichok PP, Antoshchuk AP (1977) Izv Akad Nauk Neorg Mater 13:1327
47. Phillips B, Somiya S, Muan A (1961) J Am Ceram Soc 44:167
48. Ahmed YMZ, Ewais EMM, Zaki ZI (2010) J Alloy Compd 489:269
49. Özgür Ü, Alivov Y, Morkoc H (2009) J Mater Sci Mater Electron 20:789
50. Chikazumi S (2005) Physics of ferromagnetism. Oxford University Press, Oxford
51. Krissman CJ, Harrison SE (1956) Phys Rev 103:857
52. Antic B, Jovic N, Pavlovic MB, Kremenovic A, Manojlovic D, Vucinic-Vasic M, Nikolic AS (2010) J Appl Phys 107:043525
53. Rashad MM (2007) J Mater Sci 42:5248
54. Chen C, Rondinone AJ, Chakoumakos BC, Zhang ZJ (1999) J Magn Magn Mater 194:1
55. Chen Q, Zhang ZJ (1998) Appl Phys Lett 73:3156
56. Nogues J, Schuller IK (1999) J Magn Magn Mater 192:203
57. Sepelak V, Feldhoff A, Heitjans P, Krumeich F, Menzel D, Litterst FJ, Bergmann I, Becker KD (2006) Chem Mater 18:3057
58. Sepelak V, Baabe D, Mienert D, Litterst FJ, Becker KD (2003) Scr Mater 48:961
59. Kodama RH, Makhlouf SA, Berkowitz AE (1997) Phys Rev Lett 79:1393
60. Nipan GD, Ketsko VA, Stognij AI, Trukhanov AV, Koltsova TN, Kopeva MA, Elesina LV, Kuznetsov NT (2010) Inorg Mater 46:429
61. Kim HG, Borse PH, Jang JS, Jeong ED, Jung OS, Suh YJ, Lee JS (2009) Chem Commun 39:5889
62. Kubelka P, Munk F (1931) Z Techn Phys 11:593
63. Kortüm G, Vogel J (1958) Z Phys Chem 18:110
64. Nowak M, Kauch B, Szperlich P (2009) Rev Sci Instrum 80:046107
65. McLean TP (1960) In: Gibson AF (ed) Progress in semiconductors, vol 5. Heywood, London
66. Roduner E (2006) Chem Soc Rev 35:583